Solar Energy Materials & Solar Cells 277 (2024) 113094

Contents lists available at ScienceDirect

Solar Energy Materials and Solar Cells

journal homepage: www.elsevier.com/locate/solmat

Tuning emittance in films of plasmonic metal oxide nanocrystals for daytime radiative cooling

Daniel William Davies [a,1], Benjamin J. Roman [a,1], Delia J. Milliron [a,b,*]

[a] The University of Texas at Austin, McKetta Department of Chemical Engineering, Austin, 78712, TX, United States
[b] The University of Texas at Austin, Department of Chemistry, Austin, 78712, TX, United States

ARTICLE INFO

Keywords:
Radiative cooling
Plasmonic
Nanocrystals
Metal oxide
Photovoltaics

ABSTRACT

Radiative cooling offers a passive, low-cost option for thermal management without expending energy on intensive active cooling mechanisms. Doped metal oxide nanocrystals are a promising option for maintaining high solar transparency while accessing tunable emission in the primary atmospheric transparency window from their localized surface plasmon resonance. Finite element method simulations of nanocrystal films are used to explore impacts of nanocrystal size, doping concentration, and film thickness on film emissivity. We reveal trade-offs between emission intensity and selectivity: Targeting selective emission results in unwanted reflectance from nanocrystal coupling limiting the maximum emissivity, while maximizing emissivity through increasing film thickness causes unwanted solar absorption from broadened emission. The trade-offs result in temperature-dependent design rules for optimizing radiated power. An optimized radiative cooler could provide 20 ° C of cooling, close to the ideal emitter. High emissivity is achievable in real nanocrystals which exhibit extinction peaks close to the best simulated case.

1. Introduction

Daytime radiative coolers can provide passive, electricity-free cooling, reducing the energy cost of temperature regulation. Temperature regulation, while important for operating habitable spaces, accounts for upwards of 40% of energy building usage [1,2]. To obtain effective radiative cooling under direct sunlight the material must be highly emitting in the mid to far infrared (IR), coinciding with the black body (BB) irradiance spectrum while maintaining very low solar absorption [3–6]. Additionally, for terrestrial applications, the emission must also target the IR transparency windows of Earth's atmosphere which is critical for sub-ambient cooling [3,7]. The atmospheric transparency occurs mainly in the wavelength ranges of 8-13 μm as the primary window with secondary and tertiary windows at 3-4 μm and 15-20 μm, respectively [8–10]. Thus materials with highly selective absorption (emission) are required for maximizing sub-ambient cooling. Selective absorption has been achieved through several methods such as multilayer photonic resonator structures [11–14], phonon resonance materials [7,15,16] or polymers mixed with dielectric nanoparticles [17–20]. For high surface temperatures or extraterrestrial applications the penalty from atmospheric absorption is low, thus the ideal NC film has emittance covering the entire BB spectrum [21,22]. This broad absorption has typically been accessed via nanostructured oxides such as glass [21–24] or TiO_2 [25], providing substantial emittance for high-temperature applications such as cooling of photovoltaic (PV) cells. However, these emissive materials are limited in tunability due to relying on intrinsic phonon or molecular resonances to achieve high emissivity.

Tunable emission is critical for maximizing radiative cooling targeted at specific applications depending on variables such as operating temperature and atmospheric conditions. Doped metal oxide NCs enable a pathway to synthetically tunable high emissivity via plasmonic absorption. In the mid-IR region, the localized surface plasmon resonance (LSPR) from free carrier oscillations localized to the NCs interact strongly with light, resulting in absorption and reflection at wavelengths related to the electron concentration [26,27]. Additionally, due to the wide bandgap of metal oxide materials such as indium tin oxide (ITO), NC films offer excellent transparency to solar radiation, critical to ensure low parasitic heating [28,29]. The LSPR emission of doped metal oxides is readily tunable via well established synthetic methods [29,30] by controlling parameters such as NC size [31,32], shape [33,34], dopant selection [29,30,35,36] and dopant concentration [37]. By changing the Sn dopant at.% in tin-doped indium oxide (ITO) NCs, the LSPR peak position can be shifted across the near-IR to mid-IR region through the resulting change in the free electron

* Correspondence to: 200 E Dean Keeton St, Austin, TX 78712.
E-mail address: milliron@che.utexas.edu (D.J. Milliron).
[1] These authors contributed equally.

https://doi.org/10.1016/j.solmat.2024.113094
Received 10 April 2024; Received in revised form 30 July 2024; Accepted 8 August 2024
Available online 20 August 2024

concentration [26,37]. Recently, L. Ling and Z. Chen et al. explored the potential use of doped metal oxide NCs as thermal emitters based on their LSPR [29]. They showed a variety of metal oxide NC materials hold promise for accessing emission within the primary transparency window. At the same time, the use of plasmonic metal oxide NCs has been shown to enhance the emissivity of PMMA nanocomposite films [10] where the introduction of self-doped In_2O_3 NCs obtained a net cooling power close to the theoretical limit.

While metal oxide NCs offer a versatile platform with tunable emission, design rules to maximize the cooling potential of close-packed NC films remain poorly defined. Plasmonic NC emitters have been particularly understudied in densely packed films which maximize the active material filling fraction and result in a complex set of inter-dependencies between the LSPR emission and synthetic parameters such as NC doping, size, damping and film thickness. Interacting NCs result in hybridization of nearby LSPRs resulting in collective dipole oscillations [38]. Increasing coupling between NC LSPRs leads to a significant redshift in the LSPR peak [31,38–40]. Both reflectance and absorptance contribute to the LSPR shift [38,39] and near saturation changing the ratio between absorption and reflection will significantly impact the intensity of the emission. The strength of LSPR coupling depends on a number of factors, including electron concentration, damping, and the gap:diameter ratio, resulting in a complex interdependence for controlling the LSPR absorptance to reflectance ratio [32,39]. Additionally, increasing film thickness of close-packed NCs to increase the absorptance of the film results in splitting of the reflectance peak into two different modes, further complicating the absorptance to reflectance trade-off [41–43]. Understanding these trade-offs is critical to obtaining maximum cooling performance from doped metal oxide radiative coolers.

In this work, we explore the design rules for highly emissive coatings using doped metal oxide NCs through finite element method simulations of assemblies of metal oxide NCs. By changing the NC doping, damping, size, and film thickness we found these parameters impart compromises between the reflectance and absorptance of the LSPR leading to a trade-off between the intensity and selectivity of the film emissivity. Additionally, the balance of this trade-off shifts with the operating temperature, resulting in temperature-dependent design rules for maximizing the radiative cooling potential. We then calculated the cooling effect on a photovoltaic system and compared this to a perfect emitter as the solar angle changes. The ITO NC film showed a consistent 20-30 K drop in equilibrium temperature, only ~5 K less than the perfect emitter, resulting in up to a 1.21x enhancement in photovoltaic efficiency. Finally, we demonstrate the potential for experimentally realizing coatings like those we explored computationally by fabricating low-doped ITO NC films whose peak extinction is well aligned with the main atmospheric transparency window.

2. Materials and methods

2.1. Materials

All chemicals were used without an additional purification step. The NC synthesis used indium(III) acetate (99.99%, sigma-aldrich), tin(IV) acetate (Strem), oleic acid (90% technical grade, Sigma-Aldrich), and oleyl alcohol (90% technical grade, Sigma-Aldrich). Washing the NCs and spincoating used hexane (≥ 99.9%, Fischer), ethanol (Pharmco 100% anhydrous) and octane (reagent grade, Sigma-Aldrich).

2.2. NC synthesis

NCs of ITO were synthesized using a modified previously reported slow injection method [30,44]. Precursors of Sn (IV) acetate and In (III) acetate were dissolved in 10 mL of oleic acid in a round bottom flask based on the desired Sn doping % desired. For 1% ITO, 0.048 mmol of Sn (IV) acetate and 4.752 mmol of In (III) acetate were used. For 0.5% ITO, 0.024 mmol of Sn (IV) acetate and 4.776 mmol of In (III) acetate were used. The precursor underwent degassing under vacuum for 15 min at room temperature and then heated to 80 °C where the solution was stirred under vacuum for 1.5 h. Finally, the precursor solution was heated to 150 °C under nitrogen for 2 h. In a separate flask, 13 mL of oleyl alcohol was heated under nitrogen to 290 °C. For both NC syntheses, 9 mL of the precursor solution was slowly injected into the hot oleyl alcohol at 0.2 mL min^{-1}. After injection, the NCs were obtained via precipitation using ethanol and centrifuged at 7500 rpm for 5 min. The NCs were then washed 3 times by redispersing the pellet in 10 mL hexanes, adding 100 μL each of oleyl amine and oleic acid, and then precipitating with decreasing amounts of ethanol to control size and uniformity by removing the supernatant each time. Finally, the NCs were dispersed in 7.5 mL hexanes and centrifuged for 2 min at 2000 rpm and the supernatant was kept to remove any large particles from the NCs.

2.3. Film fabrication

NC films of ITO were obtained via spin-coating NCs at 500 RPM onto double-side polished silicon wafers from a 1:1 hexane:octane solution at a concentration of 150 mg mL^{-1}. The films were placed in a bath of formic acid in acetonitrile at a concentration of 0.05 M for 30 min and subsequently washed in fresh acetonitrile. The spin coat deposition was then repeated to achieve thicker films. The film thicknesses of 548 nm and 561 nm for the 0.5% and 1% NC films were obtained via stylus profilometry.

2.4. FTIR characterization

FTIR spectra of NCs, both dispersed and film, were collected in a Bruker Vertex 70 spectrometer in transmission mode. Dispersions of 0.5% and 1% Sn ITO NCs in tetrachloroethylene were measured in transmission FTIR using a liquid cell with CaF windows. Films of ITO NCs measured using transmission FTIR were fabricated on undoped double side polished silicon substrates via the spincoating method discussed above. All samples were measured using unpolarized light at normal incidence.

3. Calculations and theory

3.1. Nanocrystal simulations

Finite element method simulations were carried out in COMSOL version 6.0 using the Wave Optics Module. The NCs' dielectric function was described using the Drude-type dielectric function

$$\varepsilon = \varepsilon_\infty - \frac{\omega_p^2}{\omega^2 - i\omega\gamma} \quad (1)$$

where ε_∞ is the high-frequency dielectric constant, ω_p is the bulk plasma frequency, and γ is the damping constant.ε_∞ was set to a value of 4 to approximate that of ITO which has been well studied previously [45–47]. While ε_∞ is dependent on the electron concentration, the simulations were performed at a low charge carrier concentration therefore a constant ε_∞ is used.

The NCs' bandgap was accounted for using the previously measured complex refractive index of an ITO NC film [28].

The NCs were arranged in a hexagonally close-packed assembly, with the c-axis normal to the plane of the film and with Floquet periodic boundary conditions along the sides of the simulation geometry. The interparticle spacing was set to 3.5 nm, and the medium surrounding the NCs was given a refractive index of 1 to correspond with air. The NCs were optically excited with p-polarized light using a periodic port at the top and bottom of the simulation geometry. p-polarized light was used in the simulations so that we could more easily examine higher angles of incidence, where s-polarized light more strongly reflects.

Including the s-polarization would reduce the overall emissivity while maintaining consistent trends (Fig. S1) concerning the design parameters investigated here. Due to increased reflectance of the s-polarized light, simulating the p-polarized light only provides a best-case scenario for maximizing P_{rad} at higher incident angles. The angle-dependent optical properties were simulated for incident angles of 0, 15, 30, 45, 60, 75, and 80 degrees relative to the normal.

3.2. Net radiative power

To evaluate the optimal design for an emitter, the net power radiated, P_{net} was calculated as

$$P_{net} = P_{rad} - P_{atm} - P_{sol} \tag{2}$$

where P_{rad}, P_{atm}, P_{sol} are the power emitted from the surface, power emitted back from the atmosphere, and solar radiation absorbed, respectively. P_{rad} was calculated by

$$P_{rad} = 2\pi A * \int_0^{\frac{\pi}{2}} \int_0^{\infty} I_{BB}(\lambda, T_s) e_r(\lambda, \theta) sin(\theta) cos(\theta)\, d\lambda\, d\theta \tag{3}$$

where A is the area, I_{BB} is the black body irradiance evaluated at the surface temperature T_s, e_r is the emissivity of the radiator, λ is the wavelength, and θ is the zenith angle [6,15]. Here, we assume the emission is symmetric with respect to the azimuthal angle and have integrated along φ, resulting in the factor of 2π. The simulated emissivity was interpolated using a cubic spline and integrated over the range 0.2-25 μm and then integrated across 7 angles from θ = 0-80° using the trapezoidal rule.

I_{BB} is given by calculated by

$$I_{BB} = \frac{2hc^2}{\lambda^5} \frac{1}{e^{\frac{hc}{\lambda k_B T_s}} - 1} \tag{4}$$

where h is Planck's constant, c is the speed of light and k_B is the Boltzmann constant. P_{atm} was calculated by

$$P_{atm} = 2\pi A * \int_0^{\frac{\pi}{2}} \int_0^{\infty} I_{BB}(\lambda, T_a) e_r(\lambda, \theta) e_a(\lambda, \theta) sin(\theta) cos(\theta)\, d\lambda\, d\theta \tag{5}$$

where T_a and e_a are the ambient temperature and angle dependent atmospheric emissivity. The angle dependent emissivity for the atmosphere was modeled at each evaluated angle using Lowtran7 using the U.S. standard atmospheric model [48,49].

$$P_{sol} = A \int_0^{\infty} I_{solar} e_r(\lambda)\, d\lambda \tag{6}$$

where I_{solar} is the solar radiance at a particular solar angle. For P_{net} calculations, a solar angle of 6.75°. The angle corresponds to the latitude of Austin, Texas at midday on the summer solstice and provides a standard to evaluate the performance of the NC films. The solar irradiance at different angles was modeled using Lowtran7.

3.3. Evaluation for PV cooling

The equilibrium temperature for a PV panel was obtained by adding in convective heat transfer and solar absorption equations terms to the P_{net} as follows:

$$P_{net} = P_{rad} - P_{atm} - P_{sol} + P_{conv} + P_{PV} \tag{7}$$

where P_{conv} and P_{PV} are the convective heat transfer and photovoltaic heating terms, respectively. The convective heat transfer was calculated by

$$P_{conv} = hA(T_s - T_a) \tag{8}$$

where h = 2.8 + $3V_{avg}$ and V_{avg} is the average wind velocity in m s^{-1} [50]. A constant V_{avg} of 1 m s^{-1} was used in all calculations. The photovoltaic heating was calculated by

$$P_{PV} = A(1 - \eta_{PV}) \int_0^{\infty} I_{solar}(\theta_s)\, d\lambda - P_{sol} \tag{9}$$

where η_{PV} is the temperature-dependent efficiency which is given by the Evans-Florschuetz PV efficiency correlation,

$$\eta_{PV} = \eta_{T_{ref}} [1 - \beta_{ref}(T_s - T_{ref})] \tag{10}$$

with $\eta_{T_{ref}}$, β_{ref}, and T_{ref} are 0.12, 0.0045 °C^{-1}, and 25 °C – typical values for silicon solar cells [51,52]. In this model, we assume the remaining solar power not converted into electricity is absorbed as heat to provide a worst case scenario for errant solar heating. Also, we subtract P_{sol} of the NC film as this light is absorbed by the NC top layer and cannot contribute to the light absorbed by the PV cell. Though we note for our case, P_{sol} for all of the NC films evaluated is less than ~5% of the total solar irradiance so this effect is small. The temperature reduction was determined by setting P_{net} = 0 for scenarios with and without the NC film. Solar efficiency was calculated at each temperature using Eq. (10).

3.4. Perfect emitter

The ideal emitter for a given T_s was calculated by

$$e_r(\lambda, T_s, T_a, \theta, \alpha) = \begin{cases} 1 & \text{if } I_{BB}(\lambda, T_s) > I_{BB}(\lambda, T_a) e_a(\lambda, \theta, \alpha) \\ 0 & \text{if } I_{BB}(\lambda, T_s) \le I_{BB}(\lambda, T_a) e_a(\lambda, \theta, \alpha) \end{cases} \tag{11}$$

4. Results

4.1. Design constraints and parameters

To achieve maximum radiative cooling under daytime conditions (Fig. 1a), the cooler must maximize P_{rad} via high emissivity in the region of BB irradiance (3-20 μm). Under ideal conditions at 300 K using the ideal emitter from Eq. (11), emitting directly to space can achieve upwards of P_{rad} = 460 W m^{-2}. However, since the maximum solar radiance is typically around 1000 W m^{-2}, low solar absorption is also critical to providing effective cooling during daytime. Additionally, terrestrial applications must consider the atmospheric transparency windows, which further restrict the potential radiative cooling and impose additional constraints based on the surface temperature. As a result, the target emission wavelengths may differ depending on the surface temperature, thermal load to be cooled, and atmospheric conditions for the application.

Doped metal oxides NCs offer a widely tunable LSPR absorption through controlling the NC synthesis and film deposition process. Through well-established protocols, we can control the Sn doping %, NC size, damping coefficient, and film thickness (Fig. 1c). Sn doping concentration strongly modulates the LSPR peak position and intensity of the plasmonic response across the mid-wave IR (MIR) wavelengths determined by the electron concentration. LSPR damping which can be controlled via methods such as dopant selection [35] which increases the full width at half maximum (FWHM) of the LSPR peak, influencing spectral selectivity. Finally, the NC film thickness can be controlled via a wide variety of solution coating techniques to increase the LSPR absorption, though deleterious solar absorption can be concomitantly increased for thicker films. The control of the LSPR peak position, intensity, and width provides a platform for developing application-targeted highly emissive NC films. Yet, the trade-offs and interdependencies of these materials tuning parameters in governing radiative cooling performance are unclear *a priori*, motivating our systematic investigation of their effects.

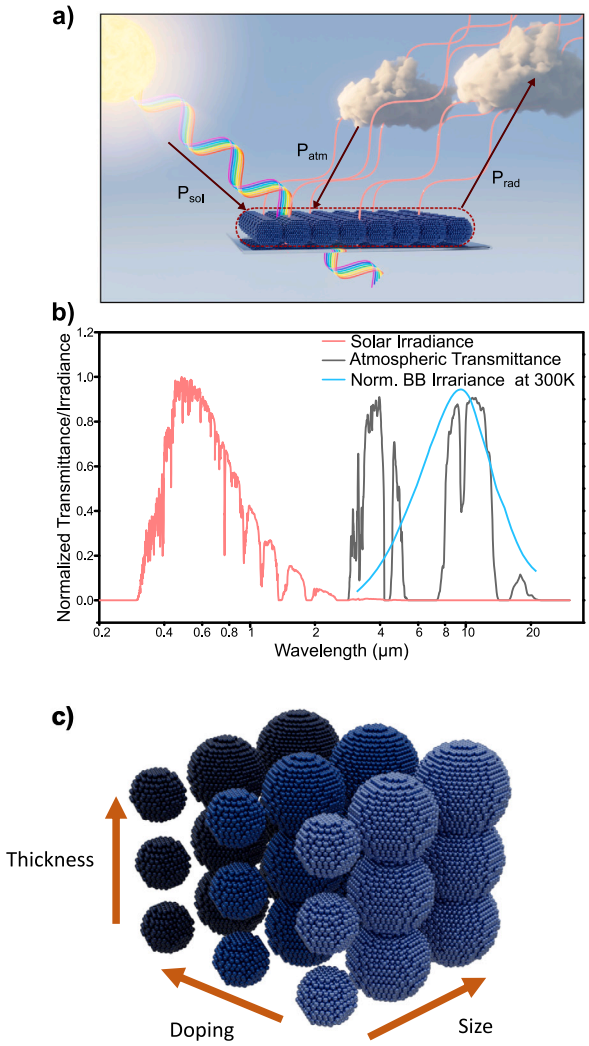

Fig. 1. (a) Schematic showing a NC film that exhibits high solar transparency and synthetically tunable emission in the mid-IR region. (b) Plot of the normalized AM 1 solar irradiance (red) calculated with Lowtran7, atmospheric transparency (gray) modeled with as the US standard atmosphere via Lowtran7, and black body irradiance spectrum (blue) calculated at 300 K by Eq. (4). (c) Schematic showing size, doping, and thickness as readily tunable parameters of NC films.

4.2. Emission trade-offs

The NC LSPR is not a purely absorptive response, as scattering processes also give rise to reflectance in NC films. As a result, how these design parameters change the ratio of absorption to reflection plays a critical role in determining the emissive behavior. To assess potential trade-offs between these parameters, finite element method simulations of the optical properties of ITO NC films were performed (see Section 3). Finite element methods have previously shown good agreement between simulated NC films and experimental close-packed film counterparts [39,53]. The NCs were arranged in hexagonal close-packed films with a constant gap of 3.5 nm. While the packing may generally be expected to impact the optical properties of the film, we note that face centered cubic packing also provides nearly identical simulated extinction spectra as seen in Fig. S2. Absorptance and reflectance were simulated across the spectrum from 0.2 to 25 μm wavelength. The absorption showed a strong plasmonic response in the mid-IR region (Fig. 2), as indicated by the electric field enhancement at resonance shown in Fig. S3. The large FWHM observed in the plasmon results from the relatively low plasma frequencies required to shift the absorption to mid-IR wavelengths. We note that the reflectance between 0.2 and 5 μm result from internal reflections related to the refractive index contrast between the NC film and air. These reflections do not appear when the NC film is coated on a substrate with a higher refractive index, as would typically be the case (Fig. S4), and they should not impact the transparency in the solar region. The dopant concentration and damping were represented in the model by setting the plasma frequency (ω_p) and damping coefficients (γ) in Eq. (1) while coupling was controlled via the NC radius through the resulting change in the gap/diameter ratio. Parameter sweeps were performed across two different thicknesses (1.9 and 5.8 μm) with other variables held constant. The simulated absorptance and reflectance spectra at normal incidence are plotted in Fig. 2.

Low-doped NCs is necessary for approximating the BB irradiance spectrum but their low electron concentration results in weak LSPR absorptance, impeding the maximum attainable emission in the desired window. The absorptance decreases and broadens substantially with lower ω_p values for the 1.9 μm film (Fig. 2a, bold). Yet, increasing the doping level to achieve a higher maximum absorptance quickly becomes counterproductive as the absorptance peak blueshifts and narrows until the emissivity falls outside the primary transparency window. On the other hand, the reduced absorption intensity from low doping may be compensated by saturating the intensity using thicker films as seen in the 5.8 μm case (Fig. 2d). However, this also reduces the spectral selectivity of the absorption, mainly in the mid-IR region above ~15 μm which corresponds with a reduction in reflectance in the region. Where in the 1.9 μm film there is broad reflectance which gradually intensifies with increasing ω_p (Fig. 2a, dashed), the 5.8 μm film exhibits a weaker reflectance peak which gradually undergoes splitting into two distinct peaks at 9 μm and 15 μm. This splitting of the reflectance peak follows observations made by Matsui and Tabata, et al. in ITO NC films, where two reflectance modes occur as distinct dipolar plasmon oscillations [42]. The higher energy mode (9 μm) occurs from out-of-phase oscillations of neighboring LSPRs whereas the lower energy mode (15 μm) is the result of in-phase dipole oscillations of the LSPRs. The peak splitting is a consequence of quadrupole interactions between different NC layers, resulting in a strong dependence on coupling between NCs. With increasing ω_p, the out-of-phase mode continues to blueshift in opposition to the in-phase mode which redshifts. When the absorptance approaches saturation, $\omega_p \geq 3000$ cm^{-1}, the increased reflectance results in corresponding dips in the absorptance at each reflectance mode. For each thickness, there is a trade-off between aligning the LSPR peak in the proper emission window and accessing the maximum intensity and selectivity for the emittance.

Decreasing LSPR damping improves the spectral selectivity of the absorptance without shifting the peak position outside the transparency window but at the cost of increased reflectance limiting the maximum attainable emission. With a decrease in damping, the width of the absorptance peak decreases concomitantly with increasing the max absorptance at the peak (Fig. 2b,e, bold). The increase in maximum absorptance in the 1.9 μm film is limited by increasing reflectance, with severe diminishing returns occurring at $\gamma \leq 750$ cm^{-1}. Despite the trade-off of maximum absorptance with reflectance, the spectral selectivity is significantly improved below $\gamma = 1000$ cm^{-1}. In the thicker 5.8 μm film where the absorptance is near saturation, decreasing γ has little impact on the maximum absorptance and even at $\gamma = 500$ cm^{-1} the absorptance is still very broad compared to the 1.9 μm film (Fig. 2e, bold). Conversely, the effects of increasing reflectance become much more pronounced in 5.8 μm film, resulting in a decrease in absorptance within the primary transparency window. The reduced emittance in the primary window, however, must be balanced with the benefits of preventing unwanted absorption from atmospheric and solar irradiance. Consequently, the benefits reaped by improved selectivity are tempered by increased reflectance which reduces the maximum

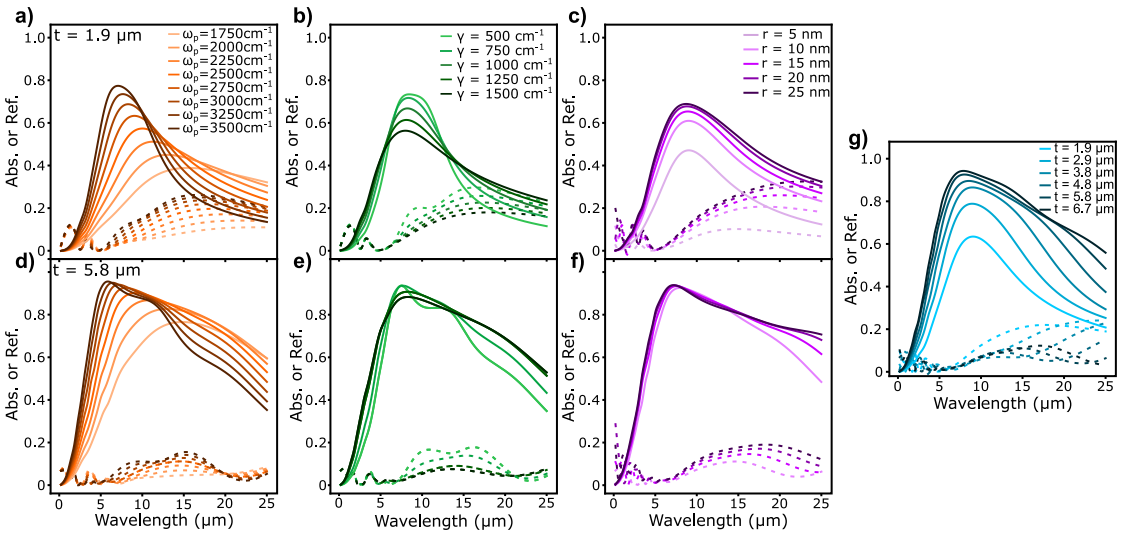

Fig. 2. Evolution of normal incident absorptance (bold) and reflectance (dashed) spectra at t = 1.9 μm for varying (a) ω_p (γ = 1000 cm^{-1}, NC radius = 10 nm), (b) γ (ω_p = 2750 cm^{-1}, NC radius = 10 nm), and (c) NC radius (γ = 2750 cm^{-1}, ω_p = 1000 cm^{-1}). Absorptance (bold) and reflectance (dashed) spectra at t = 5.8 μm for varying (d) ω_p (γ = 1000 cm^{-1}, NC radius = 10 nm), (e) γ (ω_p = 2750 cm^{-1}, NC radius = 10 nm), and (f) NC radius (γ = 2750 cm^{-1}, ω_p = 1000 cm^{-1}). (g) Absorptance (bold) and reflectance (dashed) spectra with varying thickness (γ = 2750 cm^{-1}, ω_p = 1000 cm^{-1}, NC radius = 10 nm).

obtainable absorptance. The balance of this trade-off is modulated by thickness.

Increasing NC radius leads to increased absorptance as a result of a higher fill factor for larger NCs, with little effect on peak position curtailing coupling as a method to access optimal emittance at longer wavelengths. In the thinner, 1.9 μm film case, increasing NC radius showed a marked increase in the absorptance across the calculated wavelength range without shifting the absorptance peak (Fig. 2c bold), counter to an expected redshift from increased coupling. The entirety of the redshift in the extinction (Fig. S5a,c) follows the increase and redshift of the reflectance (Fig. 2c, dashed). The driving factor for the increased absorptance with larger NCs is a concurrent increase in the NC fill factor resulting from the constant 3.5 nm gap between NCs. Once the extinction is normalized by the fill factor, most of the intensity increase is removed, leaving the effects of the higher reflectance from the increased coupling (Fig. S5b). In the thicker 5.8 μm film, a similar effect is observed in the extinction spectra: normalizing by the fill factor removes most of the increase in extinction. However, the effect of fill factor absorptance becomes much less apparent as the absorptance is already saturated, resulting in marginal alteration to the absorptance (Fig. 2f dashed). Increasing the NC size may alleviate some difficulty in accessing thicker films by reducing the impact of the NC gap, though this benefit is less significant when using NCs with a radius above 10 nm.

Increasing thickness enhances the maximum absorptance in tandem with broadening the spectral width of the LSPR absorptance, which facilitates higher emittance potential while amplifying penalties from unwanted solar and atmospheric absorption. The broadening of the absorptance peak occurs simultaneously with a redshift in the broad reflectance peak initially observed at ~15 μm in the 1.9 μm film (Fig. 2g). Considering the significant redshift of the reflectance peak into the far IR with increasing thickness, we suspect this reflectance mode likely results from geometry-related interference such as observed by Matsui et al. [41]. As the absorptance saturates, we observe the two reflectance peaks identified as LSPR out-of-phase and in-phase modes only slightly redshift by comparison, leading to the characteristic dips in absorptance at a thickness of 6.7 μm. Saturating the absorptance is critical to maximizing the power radiated, however reducing the selectivity of the absorptance will have detrimental effects from increased solar absorption as well. Controlling the film thickness offers another route to tune the maximum emittance versus spectral selectivity trade-off and compensate for low absorption from NCs tuned to access mid-IR LSPRs.

Modulating ω_p and γ together results in an additive impact on the individual trade-offs between maximum absorptance and spectral selectivity. For lower ω_p values, at 2500 and 3500 cm^{-1}, reducing the NC damping results in a smaller absorptance peak width while increasing the maximum intensity near the peak (Fig. 3a,b). However, at ω_p = 2500 cm^{-1} the reduction in peak width within the targeted wavelength range is marginal as compared to ω_p = 3500 cm^{-1}. The tempered narrowing of the absorptance at lower ω_p prevents γ from balancing the reduced selectivity caused by low electron concentrations. In contrast, for ω_p = 4500 cm^{-1}, the LSPR peak approaches saturation of the extinction which limits the increase in absorptance near the peak (Fig. 3b,c). At ω_p = 3500 cm^{-1}, this manifests as a flattening of the absorptance peak with severe diminishing returns when γ = 500 cm^{-1} resulting from an increase in reflectance at ~6 μm (Fig. 3b, dashed). When ω_p is increased to 4500 cm^{-1}, changing γ has little impact on the peak absorptance despite having enhanced modulation of the peak width. Below γ = 1000 cm^{-1}, the absorptance with decreasing γ across the wavelength range, resulting in a peak height lower than the absorptance at γ = 1500 cm^{-1} (3c). The reduction in absorption intensity is due to the enhanced response from the reflectance at higher doping levels, which appears to interact synergistically with the reflectance increase at lower γ. Altering ω_p and γ in parallel results in a convolution of individual trade-offs, preventing γ from effectively controlling the absorptance linewidth at low ω_p or intensity at high ω_p.

4.3. Radiative cooling design rules

The trade-offs between the NC film tuning parameters can be quantitatively evaluated based on how they affect the balance between the three key radiative heat transfer terms: P_{rad}, P_{atm}, and P_{sol} calculated via Eqs. (3), (5), and (6), respectively. Additionally, different material trade-offs may dominate depending on the surface temperature (T_S) and atmospheric conditions, with maximizing P_{rad} becoming more important at high temperatures and minimizing P_{atm} and P_{sol} being more important at low temperatures. We calculated the net power radiated across each of the parameter sweeps at 3 different temperatures: T_S = 300 K, T_S = 330 K, and T_S = 360 K shown in Fig. 4 bottom, middle, and top respectively. A complete breakdown of each P_{rad}, P_{atm}, and P_{sol} at 300 K can be found in Fig. S6.

ω_p dependence. By varying ω_p (Fig. 4a), we anticipated there should be an ideal ω_p value based on the trade-off between accessing the

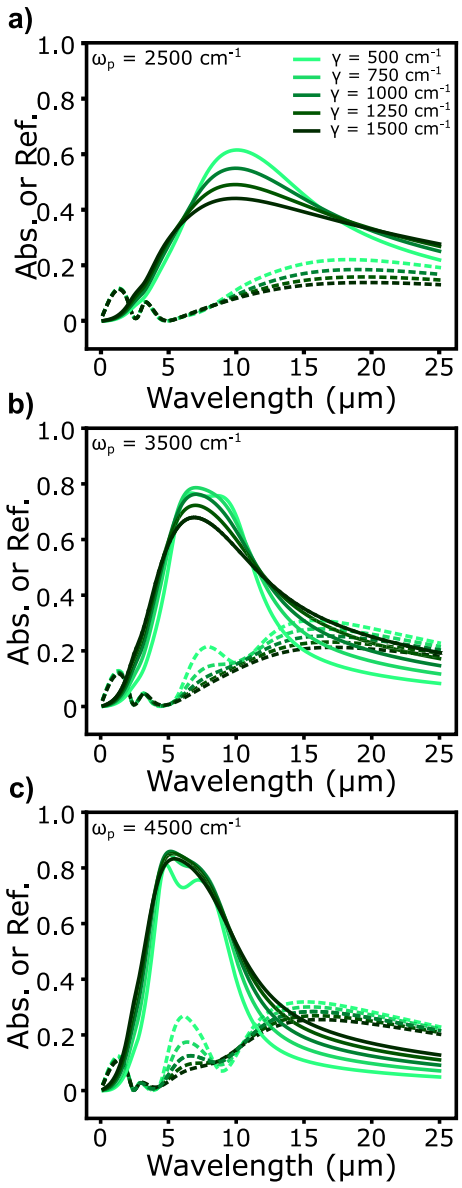

Fig. 3. Absorptance (bold) and reflectance (dashed) spectra at normal incidence with varying γ at (a) ω_p = 2500 cm^{-1}, (b) ω_p = 3500 cm^{-1}, (c) ω_p = 4500 cm^{-1}. Film thickness and NC radius for each sweep were held constant at 1.9 μm and 10 nm, respectively.

proper emission window and attaining high emissivity and selectivity. Indeed, based on our calculations, there is an optimal ω_p in the 2000-3000 cm^{-1} range for each thickness, which positions the maximum absorptance in the primary transparency window (Fig. 4a). This result is consistent with Ling and Chen et al. who calculated an ideal ω_p of ~2400 cm^{-1} [29], though because we are accounting for the solar absorption from both the LSPR and bandgap, we identify a lower ideal ω_p value to minimize unwanted plasmon absorption in the solar region. Additionally, the thicker 5.8 μm film showed the max ω_p was redshifted as compared to the 1.9 μm at every temperature. This reflects how, while the 5.8 μm thickness compensates for reduced absorption at lower ω_p, the film sustains penalties from increased solar absorption at higher ω_p. In fact, the penalty from P_{sol} from increasing ω_p was much more severe in the 5.8 μm film than the 1.9 μm film, reducing the net power radiated by up to 50 W m^{-2} at ω_p = 3500 cm^{-1} (Fig. S6k). Moreover, the competition between P_{rad} and P_{sol} resulted in a crossover point at ω_p = 2500 cm^{-1} (Fig. 4a, bottom). Below ω_p = 2500 cm^{-1}, the thicker 5.8 μm film results in a higher P_{net} due to maximizing the absorptance in the primary window. Conversely, Above ω_p = 2500 cm^{-1}, the 1.9 μm thick film exhibits superior performance owing to reduced solar absorption. Despite having 3x more volume of NCs, at 300 K the 5.8 μm film only increased the P_{net} by only 4 W m^{-2} over the thinner film due to the parasitic solar absorption.

At higher temperatures, the P_{rad} term begins to dominate (P_{rad} >> P_{sol}, P_{atm}) as the BB irradiance of the surface increases. Above T_s = 300 K, the 5.8 μm film out competes the 1.9 μm across all ω_p values (Fig. 4 middle, top) due to the 5.8 μm film exhibiting broader absorption and capturing more of the elevated BB irradiance as well as the tempered importance of P_{sol}. Additionally, with increasing temperature there is a consistent blueshift in the optimal ω_p which approaches the BB irradiance peak as the impact from atmospheric and solar absorption effects become less important to the optimization. Even at higher temperatures, selecting the wrong ω_p still incurs sharp fall-offs away from the optimal ω_p due to missing out on potential emission from the BB peak. Thus the ω_p for an ideal radiative cooler needs to be adjusted to target the specific T_S at which the cooler will be operating.

γ dependence. γ modulation showed a trade-off between the spectral selectivity and intensity of the absorption. However, we observe that for both film thicknesses, at T_s = 300K the best emitter has γ of 500 cm^{-1}, or as low as possible (Fig. 4b, bottom). Favoring lower damping suggests spectral selectivity is significantly more important than maximizing the emissivity owing to the necessity of reducing parasitic solar absorption. While P_{rad} does show optimal γ of 750 cm^{-1} and 1250 cm^{-1} for the 1.9 and 5.8 μm films, respectively (Fig. S6b), the loss from P_{sol} outpaces any losses due to the absorptance-reflectance trade-off at low γ values (Fig. S6I). Even when ω_p is increased to 4500 cm^{-1}, it exhibited the strongest trade-off between absorptance and reflectance (Fig. 4c, bottom). At 300K the ideal emitter should select for the lowest possible damping to reduce unwanted absorption. Once the surface temperature is increased above ambient, the balance shifts away from enhancing selectivity towards maximizing emissivity. At 360K, the 5.8 μm film shows a noticeable drop in performance at γ = 500 cm^{-1} due to the absorptance-reflectance trade-off in P_{rad} now dominating (Fig. 4b, top). Additionally, we start to observe a peak in the γ dependece for NCs with ω_p > 3000 cm^{-1} for T_s = 300 K, which shifts to larger γ values at 260K. With higher temperatures, the resulting coupling of the absorptance-reflectance trade-off from both ω_p and γ is observed in Fig. 3. However, the highest performing NC films in this range of temperatures (where ω_p = 3000 cm^{-1}) still perform better at lower γ ~500-1000 cm^{-1}. For most applications, selective emission around the BB irradiance peak is ideal to prevent unwanted absorption. However, under ideal scenarios where P_{sol} is minimized or negligible, tuning the absorptance width by increasing γ captures more of the BB irradiance while simultaneously reducing unwanted reflectance.

NC radius dependence. The effect of NC radius on absorptance is dominated by changes in the fill factor of the NC film, which results in a slight increase in emission at larger NC sizes at the expense of the absorption selectivity. Consequently, the increased coupling from the larger-sized NCs does not play an impactful role in the radiative performance as coupling mainly affected the film reflectance. Increasing the NC radius, however, does improve the fill factor from 0.3 at 5 nm to 0.6 at 25 nm, which will plateau at the maximum fill factor of 0.74 for a close-packed film. The result of the increased fill factor is a general increase in absorption similar to adding thickness. When the absorption is still not saturated, as in the 1.9 μm film, there is a slight performance boost with increasing NC radius from 5 to 10 nm, but net cooling power quickly levels off at larger radii (Fig. 4d, dashed). This trend holds true for each of the calculated temperatures. The plateau in P_{net} is a result of diminishing returns in the fill factor and the nonselective increase in absorptance leading to more parasitic solar absorption in films of larger NCs. The increasing solar absorption becomes dominant in the thicker 1.9 μm film, where increasing NC radius offers no benefit

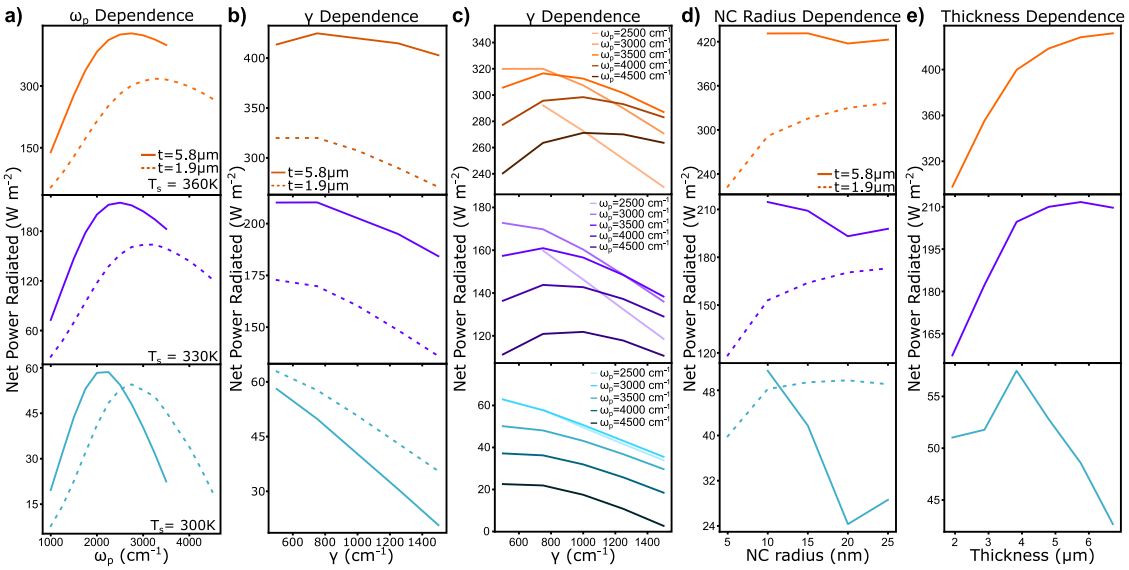

Fig. 4. P_{net} calculated at 300 K (bottom), 330 K (middle), and 360 K (top) for parameter sweeps across (a) ω_p (γ = 1000 cm^{-1}, NC radius = 10 nm), (b), (c) γ, (d) NC radius (ω_p = 2750 cm^{-1} γ = 1000 cm^{-1}) and (e) film thickness (ω_p = 2750 cm^{-1} γ = 1000 cm^{-1}, NC radius = 10 nm).

(Fig. 4d, bold). However, at higher temperatures where P_{sol} becomes less important, the difference between P_{net} of different NC radii is < 8 W m^{-2} (a less than 1% decrease in performance). While increasing the fill factor to improve the absorptance of thinner films may improve manufacturability and reduce material costs, once the absorption is maximized, further NC size increases only hinder the cooling power through parasitic heating losses.

Thickness dependence. NC film thickness is pivotal in accessing maximum emittance within the primary emission window in exchange for reduced selectivity. Increasing thickness presents an evident route to compensating for insufficient absorptance of NCs constrained to low ω_p. However, due to the broadening of the absorptance, relying entirely on thickness to offset the weak absorption leads to severe penalties from P_{sol} and P_{atm}. Particularly at low temperatures, where P_{sol} and P_{atm} dominate, adding additional NCs becomes a hindrance rather than a benefit (Fig. 4e, bottom). At T_s = 300 K, with constant NC radius = 10 nm, ω_p = 2750 cm^{-1} and γ = 1000 cm^{-1}, the optimal thickness occurs at 3.8 μm. We observe that P_{rad} exhibits diminishing returns with increasing thickness whereas P_{sol} scales linearly with thickness, resulting in a point where solar absorption dominates (Fig. S6). Notably, this peak occurs just before the effects of saturation begin to flatten the absorptance peak (Fig. 2g), representing a turning point where the emissivity gains are offset by unwanted absorption in the solar region. Identifying the critical thickness is also dependent on the other chosen parameters such as ω_p or γ which affect the LSPR intensity and, consequently, modify the critical thickness. With increasing temperature, the optimal thickness increases to higher values (Fig. 4e, middle, top). At T_s = 330 K, the optimal thickness is 5.8 μm and by T_s = 360 K the peak has shifted outside of the range we investigated. However, we expect the maximum to still occur due to the diminishing returns in P_{rad} and the linear scaling of P_{sol}. Additionally, the maximum possible solar absorption is ~ 1000 W m^{-2}, still much higher than the cooling potential from BB irradiance at 360K which places an eventual hard limit on the maximum thickness. Ultimately, increasing thickness yields ample emittance in the primary window and reduces unwanted reflectance, achieving high performance for above ambient temperature applications. However, these benefits come at the cost of reduced selectivity, impeding low-temperature performance. Fine tuning the thickness for each NC film may facilitate enhanced emittance while minimizing the effects of absorption outside the primary window.

Extraterrestrial applications. For space-based applications, the lack of an atmosphere shifts the balance of the intensity-selectivity trade-off towards maximizing intensity (P_{rad}). As such, trade-offs increasing the reflectance of the LSPR having markedly more impact on the net radiative cooling power. Additionally, the lack of an atmosphere alleviates the restrictions on BB emission, allowing more of the BB spectrum to be utilized. To evaluate these differences, we excluded the P_{atm} term and utilized the extraterrestrial AM0 solar spectrum in place for P_{sol} (Eq. (6)). We assumed direct solar incidence to consider the maximum cooling potential under the worst-case scenario. In the ω_p dependence, we no longer observe a crossover between the 1.9 μm 5.8 μm, even at T_s = 300 K (Fig. S7a). The broader absorption of the 5.8 μm film is no longer penalized compared to the terrestrial case, and, as a result, the difference in cooling potential between the two films at the maximum ω_p is nearly 100 W m^{-2}, a stark difference compared to the 4 W m^{-2} that separates the films in terrestrial performance. Additionally, without the hindrance of the atmospheric absorption, the maximum ω_p values blue shifts compared to the terrestrial case due to no penalties from atmospheric absorption. With increasing surface temperature, the ideal ω_p closely mirrors the blueshift in BB emission. Rather than highly selective emission, accessing high emissivity across the entire black body spectrum is ideal, leading to an optimal γ of 750 cm^{-1}.

Design Rules. The design targets for maximizing P_{net} depend on carefully balancing the material trade-offs affecting P_{rad}, P_{atm}, and P_{sol} which are dependent on the operating temperature and atmospheric conditions of the radiative cooler. We evaluate the design rules for three different scenarios. 1. *For low thermal loads,* where the surface temperature is close to or below ambient temperature, the ideal emitter should be highly selective towards emission within the transparency windows (Fig. S8c). At temperatures below 280 K, absorption even the tertiary window becomes undesirable due to the intensity of thermal emission from the atmosphere. The most critical parameters are ω_p and γ to ensure maximum emissivity in the primary atmospheric window and high selectivity to minimize solar absorption. The optimal dopant at.% will depend on the film thickness which is constrained to balance the trade-off between selectivity of emission outside and accessing maximum emission within the atmospheric windows. Due to needing high selectivity, the γ should always be minimized as the trade-off of increased unwanted reflectance at γ < 1000 cm^{-1} limiting P_{rad} is small compared to the penalty of increased atmospheric and solar absorption (P_{atm} and P_{sol}). 2. *For high thermal loads,* where the surface temperature is constantly above ambient temperature, the ideal emitter emits over a broad wavelength region, capturing the entire BB irradiance peak (Fig. S8a,b). To achieve broad emission with metal oxide NCs, the ideal

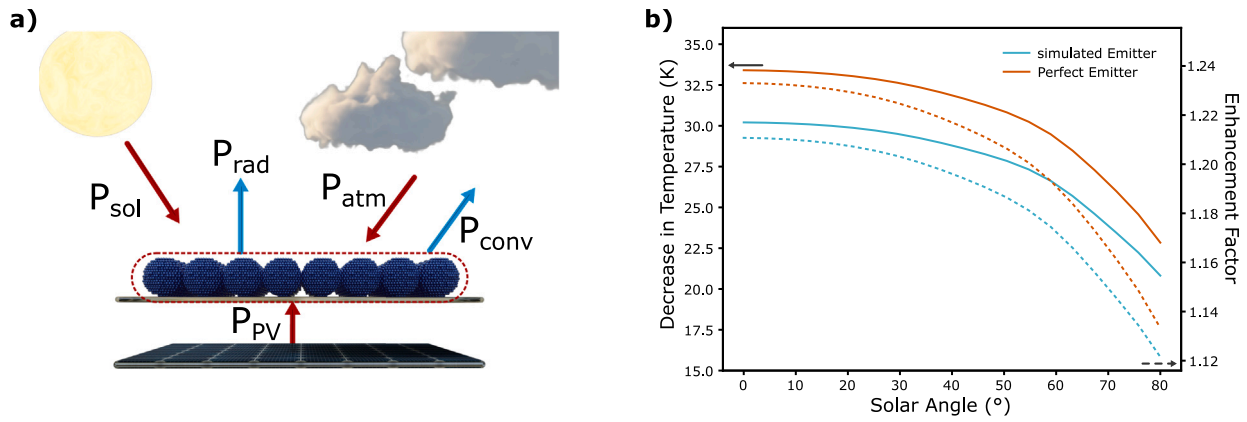

Fig. 5. (a) Schematic representation of an ITO NC film cooling a photovoltaic. (b) Calculation of the equilibrium temperature (bold) and efficiency enhancement (dashed) for the best ITO NC film simulated here (blue) and an ideal emitter (orange).

parameters will shift towards lower doping levels and make up for the decreased emittance by increasing film thickness as compared to the low-temperature case. Lower doping takes advantage of broader absorption, which should be further enhanced by increasing the γ to 750 cm^{-1} which further increases the linewidth of the absorptance and prevents unwanted reflectance. However, The NC radius should be large enough to ensure a high fill factor, but not so large that it increases solar absorptance-–10 nm is ideal, in the case of ITO. 3. *Space-based applications* also benefit from broad absorption, similar to high thermal loads. Maximizing absorption via higher thickness is the ideal strategy, while constraining the NC doping to access maximum emittance near the BB irradiance. The γ should be 750 cm^{-1} to reduce unwanted reflectance and while choosing a NC radius that maximizes the fill factor performs slightly better, the size has little influence on the resulting cooling performance.

4.4. Radiative cooling of a solar cell

To illustrate one possible application, we used these design rules to simulate the cooling potential for a NC film coated on a solar cell (Fig. 5a). The transparency of the ITO NCs to solar radiation in the visible and near-IR is essential to avoid degrading the performance of the solar cell. For these calculations, we added the convective heat transfer to the surroundings as well as heating due to absorption of the solar cell, as discussed in 3. Here, we set $P_{net} = 0$ and solve for the equilibrium temperature of the radiative cooler. To simplify the model, the temperature of the PV cell was assumed to be the same as the temperature of the radiative cooler. While there may in reality be an offset between the PV nominal operating temperature and that of the radiative cooler due to thermal contact resistance, we expect this effect to be small. Heat conduction through the NC film was also considered but resulted in a negligible (< 0.01 $W\,m^{-2}$) change in the cooling potential despite using low estimates for the thermal conductivity. Using this model, the equilibrium temperature was calculated both with and without the radiative cooler present on the surface and the difference provides the estimated temperature reduction caused by the radiative cooler. Finally, because photovoltaic cells operate more efficiently at lower temperatures, this temperature reduction was converted to an efficiency increase for the solar cell by following Eq. (10).

For a solar cell, the expected surface temperature is substantially above the ambient temperature, up to 50 °C. Thus, we selected the film parameters to maximize the radiative cooling potential at high temperatures: ω_p = 2750 cm^{-1}, γ = 750 cm^{-1}, thickness = 5.9 μm, and NC radius = 10 nm. This film provided maximum absorptance across the entire BB irradiance spectra and resulted in the max P_{net} at 360 K. This optimal NC film was compared to the ideal emitter as defined by Eq. (11). We simulated the film's performance for varied solar azimuth angles, calculating the predicted temperature reduction (bold) and photovoltaic efficiency enhancement factor (dashed) (Fig. 5). Under direct sunlight, the ITO NC film can reduce the maximum surface temperature by up to 30 K. Despite not fully optimizing the film, the NC film falls short by only 5 degrees of the cooling provided by an ideal emitter. That 30 K reduction in temperature translates to a 1.24x increase in power conversion efficiency. Even as the sun sets and approaches the horizon, the ITO NC film still maintains a 20 K temperature reduction. The increase in efficiency from reducing the PV temperature does come at a cost of some absorption of solar radiation by the NC film. However, the total solar radiation absorbed from the NC film is 30 $W\,m^{-2}$ and the majority of this falls either at the bandgap of the ITO or in the NIR region where a silicon PV system will be less efficient in any case. While the expected gains in PV efficiency are expected to outweigh the impact of reduced transparency in these regions, to fully understand the effect of this trade-off would require analyzing various specific PV systems. With a more detailed optimization routine, a NC film can be designed to maximize the cooling potential for various intended applications.

4.5. Potential and outlook

The wide tunability of metal oxide NCs offers a platform to target both subambient cooling and high temperature heat dissapation. To experimentally demonstrate the potential of metal oxide NC films to achieve properties suitable for radiative cooling, ITO NCs were synthesized using a slow injection method according to methods described above (Section 2) and are shown in Fig. 6a. Using slow injection the NC Sn at.% is easily tunable via adjusting the ratio of the indium and tin precursors, which are combined prior to injection in the reaction flask [26,32]. The extinction spectra redshifted for the films (bold) as compared to the dispersions (dashed) due to LSPR coupling within the close-packed films (Fig. 6b). We note the films measured for the 0.5% and 1% Sn doped ITO NCs were only 548 and 561 nm thick, respectively, and do not approach the saturation of the absorptance from the significantly thicker films considered in simulations. However, tuning the composition allowed us to shift the plasmon peak across the primary and secondary windows, achieving a peak near the center of the 8-13 μm window for 0.5% Sn doped NCs with a diameter of 13.9 ± 1.6 μm.

While finite elements simulations have shown good agreement with experimentally synthesized NC films [38,39,54], key differences are expected between the simulated geometry and experimental NC films. Unlike the simulated NC films, the optical properties of real films are also affected by surface depletion, NC packing, and inhomogeneity of shape and size [32,36,55,56]. Though the effects of disorder on far-field behavior are typically small [57], the additional peak width may be beneficial to realizing emissivity across the entire BB spectrum. To

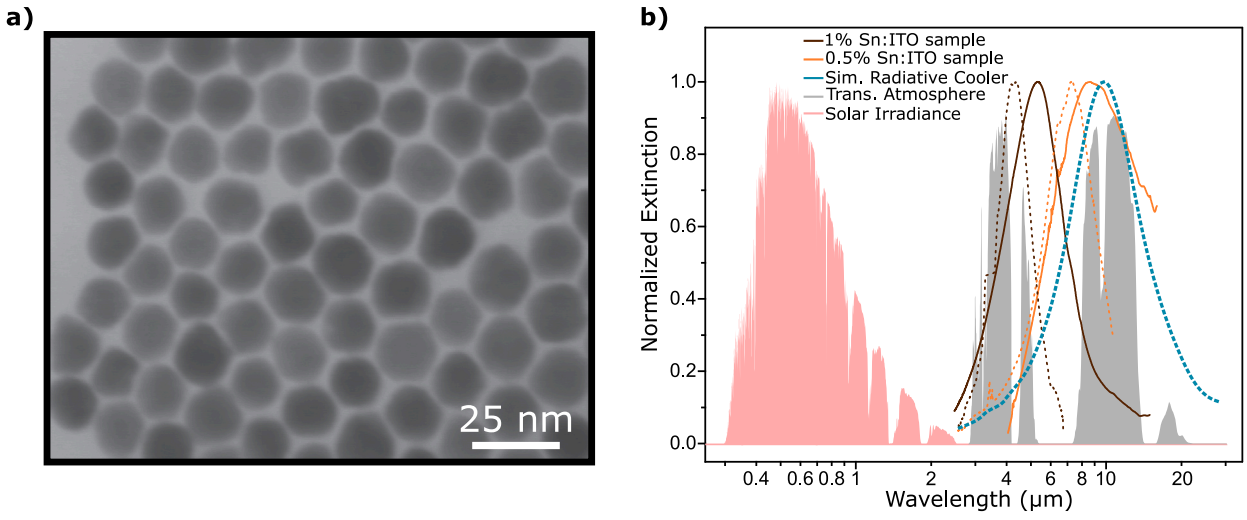

Fig. 6. (a) Scanning transmission electron microscope image of 0.5% Sn ITO NCs (b) FTIR spectra of 1% (brown) and 0.5% (orange) Sn doped ITO NCs in dispersion (dotted) and films (bold) compared with the simulated film (blue) from Fig. 5 with solar radiance under direct incident light, AM 1 (red) and atmospheric transparency (gray) spectra. The spectra were normalized to their respective maximum intensities. The diameters of the 0.5 and 1% Sn doped NCs are 13.9 ± 1.6 nm and 14.2 ± 2.9 nm, respectively.

directly compare with the measured spectra of the ITO NC films, the simulated extinction spectrum was calculated as $-log_{10}(T)$ for the best performing film analyzed in Fig. 5 (ω_p = 2750 cm^{-1}, γ = 750 cm^{-1}, thickness = 5.9 μm, and NC radius = 10 nm). At 0.5% Sn:ITO the peak extinction is close to the best simulated film for the photovoltaics application (Fig. 6b orange, blue). Though, the ideal peak position according to our design rules should be slightly redshifted compared to the 0.5% Sn:ITO NCs, ensuring minimal solar absorption. The plasmon peak can be further redshifted through synthesizing even lower doped NCs or even using plasmonic In_2O_3 where oxygen vacancies give rise to lower electron concentrations than typically found in ITO [10,58]. With fine tuning, the performance of the simulated film should be readily achievable in ITO NC films.

Accessing subambient cooling, however, will require additional optimization of the film fabrication geometry to limit solar absorption at low temperatures. Despite shifting the plasmon absorption of the ITO NCs into the desired primary transparency window, γ values typically around 1000 cm^{-1} and additional effects from inhomogeneity of the NCs increasing the plasmon linewidth, so achieving the high selectivity necessary for low-temperature applications is challenging. Even our best-simulated film using a γ = 500 cm^{-1} achieved a mediocre 68 W cm^{-2}, nearly half of the theoretical maximum for the ideal emitter. The poor performance results from the parasitic atmospheric and solar absorption in thicker films (Fig. 4) [6,10]. Thus, moving to materials with higher quality factors to achieve narrower linewidth is imperative to achieve the highly selective emission required for sub-ambient applications [33]. Alternatively, resonator geometries offer an opportunity to enhance the LSPR absorption [59–61], allowing for perfect absorption even with a monolayer of the NCs. However, the narrow linewidth of the resonator geometry may require additional strategies to access emission across the full primary transparency window, such as mixed NC structures [62].

Along with synthetically tunable emittance, metal oxide NC absorption is modulated by the free electron concentration, which provides an opportunity for dynamic emissivity via electrochemical modulation. Such dynamic control is critical for extraterrestrial applications where emission is the only means to regulate temperature [63,64]. For broad emission in the solar cell application or extraterrestrial applications, our simulated NCs showed good performance, approaching that of the ideal case in Fig. 5b. Typically dynamic emissivity has been achieved through passive control based on thermal phase change materials such as VO_2, which switches spontaneously between a transparent insulating phase and a highly emissive lossy metal phase [65,66]. On the other hand, metal oxide NCs have been shown to dramatically change plasmon extinction and position by dynamically controlling the electron concentration through chemical means [67], electrochemical modulation [55,68–71] or photodoping [72,73], providing direct control of the absorptance. Recently, work by Jia and Cheng et al. showed the potential for electrochemical modulation to control the emissivity in aluminum-doped zinc oxide NC films by switching between high and low emissive states offering 6 °C difference between them when the film is oxidized or reduced, respectively [74,75]. Achieving dynamic control of emissivity in NC films through electrochemical methods facilitates continuous targeting of specific temperatures, overcoming limitations of static emissive designs.

5. Conclusions

We have investigated the potential of doped metal oxide NC films as a daytime radiative cooler by simulating NC films with varying ω_p (doping), γ (damping), NC radius, and film thickness. We observed significant interdependencies, so the material attributes cannot be optimized one-by-one, but should instead be considered holistically. By tuning doping and damping, a trade-off between absorptance and reflectance requires a compromise between accessing maximum emissivity and highly selective emission. As such, while high doping and low damping improved spectral selectivity, which is limited by increased unwanted reflectance, reducing doping or increasing damping requires substantial increases in thickness to achieve maximum emittance leading to absorption far outside of the desired windows. The NC radius provides some improvement for low absorptance via control of the fill factor, but the increased coupling provided little benefit to accessing higher absorptance without resulting in the trade-offs discussed previously.

Understanding the interdependencies of the absorptance-reflectance and intensity-selectivity trade-offs is critical to developing design rules to maximize the radiative cooling potential of the ITO NC films. While the optimal plasma frequency is generally confined to the primary transparency window, there is a slight red shift with increasing film thickness due to reduced absorptance selectivity reflecting the higher penalty from solar absorption. Moreover, the balance of the trade-offs and their effect on the net cooling power is also dependent on the operating temperature of the NC film. For low temperatures, the NC films need to employ high selectivity to maximize absorptance in the transparency window. Such applications can take advantage of thinner films with larger NCs and their damping should be minimized.

However, the precise values to choose will depend on the balance between the expected surface temperature range and the thermal load. Thus the optimal design uses thinner films with the least damping and dopant at.% which centers the plasmon resonance peak in the transparency window. For high-temperature or extraterrestrial applications, the ideal NC film utilizes the broadband emission achieved from lower doping and higher damping levels and compensates for the reduced absorptance by maximizing the film thickness. The NC radius does not play a significant role in obtaining the maximum emittance under these conditions. When selectivity is no longer required, minimizing the loss from unwanted reflectance achieves maximum emittance.

Applying the design rules to select the film best suited for cooling a solar cell, we calculated the net cooling potential and efficiency enhancement of a solar cell. Even in a non-optimized condition, the radiative cooling provided a decrease in temperature of only 5 K less than a perfect emitter. However, for low-temperature considerations, metal oxide NCs underperform compared to other radiative cooling counterparts and achieve less than half of the theoretical radiated power. Improving the radiative cooling potential for NCs requires overcoming the trade-off between selectivity and maximizing absorptance with very low-damped NCs or coupling the LSPR with a cavity resonator. Despite the challenges, doped metal oxide NCs present an opportunity for realizing dynamically controllable emissive devices and offer a flexible platform for developing application-targeted high-emissivity coatings.

CRediT authorship contribution statement

Daniel William Davies: Writing – original draft, Software, Investigation, Formal analysis, Conceptualization. **Benjamin J. Roman:** Writing – review & editing, Writing – original draft, Software, Methodology, Investigation, Formal analysis. **Delia J. Milliron:** Writing – review & editing, Writing – original draft, Supervision, Project administration, Funding acquisition, Conceptualization.

Declaration of competing interest

The authors declare they have no financial interests orpersonal relationships that could have appeared to influence this work.

Data availability

Data will be made available upon request.

Acknowledgments

This work was supported by the National Aeronautics and Space Administration, United States through the Jet Propulsion Lab (contract 1692380), by the National Science Foundation, United States (CHE-2303296), and by the Welch Foundation, United States (F-1848).

Appendix A. Supplementary data

Supplementary material related to this article can be found online at https://doi.org/10.1016/j.solmat.2024.113094.

References

[1] D.K. Bhamare, M.K. Rathod, J. Banerjee, Passive cooling techniques for building and their applicability in different climatic zones—The state of art, Energy Build. 198 (2019) 467–490, http://dx.doi.org/10.1016/j.enbuild.2019.06.023.

[2] W. Su, P. Cai, J. Darkwa, M. Hu, G. Kokogiannakis, C. Xu, L. Wang, Review of daytime radiative cooling technologies and control methods, Appl. Therm. Eng. 235 (2023) 121305, http://dx.doi.org/10.1016/j.applthermaleng.2023.121305.

[3] C.G. Granqvist, A. Hjortsberg, Radiative cooling to low temperatures: General considerations and application to selectively emitting SiO films, J. Appl. Phys. 52 (6) (1981) 4205–4220, http://dx.doi.org/10.1063/1.329270.

[4] A.P. Raman, M.A. Anoma, L. Zhu, E. Rephaeli, S. Fan, Passive radiative cooling below ambient air temperature under direct sunlight, Nature 515 (7528) (2014) 540–544, http://dx.doi.org/10.1038/nature13883.

[5] E.A. Goldstein, A.P. Raman, S. Fan, Sub-ambient non-evaporative fluid cooling with the sky, Nat. Energy 2 (9) (2017) 1–7, http://dx.doi.org/10.1038/nenergy.2017.143.

[6] S. Jeon, J. Shin, Ideal spectral emissivity for radiative cooling of earthbound objects, Sci. Rep. 10 (1) (2020) 13038, http://dx.doi.org/10.1038/s41598-020-70105-y.

[7] Z. Chen, L. Zhu, A. Raman, S. Fan, Radiative cooling to deep sub-freezing temperatures through a 24-h day–night cycle, Nature Commun. 7 (1) (2016) 13729, http://dx.doi.org/10.1038/ncomms13729.

[8] Q. Zhang, S. Wang, X. Wang, Y. Jiang, J. Li, W. Xu, B. Zhu, J. Zhu, Recent progress in daytime radiative cooling: Advanced material designs and applications, Small Methods 6 (4) (2022) 2101379, http://dx.doi.org/10.1002/smtd.202101379.

[9] B. Bhatia, A. Leroy, Y. Shen, L. Zhao, M. Gianello, D. Li, T. Gu, J. Hu, M. Soljačić, E.N. Wang, Passive directional sub-ambient daytime radiative cooling, Nature Commun. 9 (1) (2018) 5001, http://dx.doi.org/10.1038/s41467-018-07293-9.

[10] R. Zhu, D. Hu, Z. Chen, X. Xu, Y. Zou, L. Wang, Y. Gu, Plasmon-enhanced infrared emission approaching the theoretical limit of radiative cooling ability, Nano Lett. 20 (10) (2020) 6974–6980, http://dx.doi.org/10.1021/acs.nanolett.0c01457.

[11] S. Fan, A. Raman, Metamaterials for radiative sky cooling, Natl. Sci. Rev. 5 (2) (2018) 132–133, http://dx.doi.org/10.1093/nsr/nwy012.

[12] Y. Zhang, X. Chen, B. Cai, H. Luan, Q. Zhang, M. Gu, Photonics empowered passive radiative cooling, Adv. Photonics Res. 2 (4) (2021) 2000106, http://dx.doi.org/10.1002/adpr.202000106.

[13] T. Liu, J. Takahara, Ultrabroadband absorber based on single-sized embedded metal-dielectric-metal structures and application of radiative cooling, Opt. Express, OE 25 (12) (2017) A612–A627, http://dx.doi.org/10.1364/OE.25.00A612.

[14] X. Liu, T. Tyler, T. Starr, A.F. Starr, N.M. Jokerst, W.J. Padilla, Taming the blackbody with infrared metamaterials as selective thermal emitters, Phys. Rev. Lett. 107 (4) (2011) 045901, http://dx.doi.org/10.1103/PhysRevLett.107.045901.

[15] P.R. Wray, M.P. Su, H.A. Atwater, Design of efficient radiative emission and daytime cooling structures with Si_3N_4 and SiO_2 nanoparticle laminate films, Opt. Express, OE 28 (24) (2020) 35784–35794, http://dx.doi.org/10.1364/OE.408845.

[16] H. Ma, K. Yao, S. Dou, M. Xiao, M. Dai, L. Wang, H. Zhao, J. Zhao, Y. Li, Y. Zhan, Multilayered SiO2/Si3N4 photonic emitter to achieve high-performance all-day radiative cooling, Sol. Energy Mater. Sol. Cells 212 (2020) 110584, http://dx.doi.org/10.1016/j.solmat.2020.110584.

[17] J. Peoples, X. Li, Y. Lv, J. Qiu, Z. Huang, X. Ruan, A strategy of hierarchical particle sizes in nanoparticle composite for enhancing solar reflection, Int. J. Heat Mass Transfer 131 (2019) 487–494, http://dx.doi.org/10.1016/j.ijheatmasstransfer.2018.11.059.

[18] M. Chen, D. Pang, H. Yan, Colored passive daytime radiative cooling coatings based on dielectric and plasmonic spheres, Appl. Therm. Eng. 216 (2022) 119125, http://dx.doi.org/10.1016/j.applthermaleng.2022.119125.

[19] X. Li, J. Peoples, Z. Huang, Z. Zhao, J. Qiu, X. Ruan, Full daytime sub-ambient radiative cooling in commercial-like paints with high figure of merit, Cell Rep. Phys. Sci. 1 (10) (2020) 100221, http://dx.doi.org/10.1016/j.xcrp.2020.100221.

[20] X. Li, J. Peoples, P. Yao, X. Ruan, Ultrawhite BaSO4 paints and films for remarkable daytime subambient radiative cooling, ACS Appl. Mater. Interfaces 13 (18) (2021) http://dx.doi.org/10.1021/acsami.1c02368.

[21] L. Zhu, A. Raman, K.X. Wang, M.A. Anoma, S. Fan, Radiative cooling of solar cells, Optica, OPTICA 1 (1) (2014) 32–38, http://dx.doi.org/10.1364/OPTICA.1.000032.

[22] Y. Sun, Z. Zhou, X. Jin, X. Sun, M.A. Alam, P. Bermel, Radiative cooling for concentrating photovoltaic systems, in: Thermal Radiation Management for Energy Applications, vol. 10369, SPIE, 2017, pp. 25–34, http://dx.doi.org/10.1117/12.2273916.

[23] X. Chen, Y. Gu, Designing surface microstructure for improving energy efficiency of SiO2 glass window by infrared emission, Energy Build. 304 (2024) 113838, http://dx.doi.org/10.1016/j.enbuild.2023.113838.

[24] X. Sun, T.J. Silverman, Z. Zhou, M.R. Khan, P. Bermel, M.A. Alam, Optics-based approach to thermal management of photovoltaics: Selective-spectral and radiative cooling, IEEE J. Photovolt. 7 (2) (2017) 566–574, http://dx.doi.org/10.1109/JPHOTOV.2016.2646062.

[25] M. Zahir, M. Benlattar, Design of radiative cooler based on porous TiO_2 for improving solar cells' performance, Appl. Opt., AO 60 (2) (2021) 445–451, http://dx.doi.org/10.1364/AO.413041.

[26] A. Agrawal, S.H. Cho, O. Zandi, S. Ghosh, R.W. Johns, D.J. Milliron, Localized surface plasmon resonance in semiconductor nanocrystals, Chem. Rev. 118 (6) (2018) 3121–3207, http://dx.doi.org/10.1021/acs.chemrev.7b00613.

[27] I. Kriegel, F. Scotognella, L. Manna, Plasmonic doped semiconductor nanocrystals: Properties, fabrication, applications and perspectives, Phys. Rep. 674 (2017) 1–52, http://dx.doi.org/10.1016/j.physrep.2017.01.003.

[28] R.J. Mendelsberg, G. Garcia, D.J. Milliron, Extracting reliable electronic properties from transmission spectra of indium tin oxide thin films and nanocrystal films by careful application of the Drude theory, J. Appl. Phys. 111 (6) (2012) 063515, http://dx.doi.org/10.1063/1.3695996.

[29] L. Ling, R. Zhu, Y. Gu, Z. Chen, Doped semiconductor nanoparticles for possible daytime radiative cooling applications, Semicond. Sci. Technol. 35 (7) (2020) 075018, http://dx.doi.org/10.1088/1361-6641/ab8901.

[30] A.W. Jansons, J.E. Hutchison, Continuous growth of metal oxide nanocrystals: Enhanced control of nanocrystal size and radial dopant distribution, ACS Nano 10 (7) (2016) 6942–6951, http://dx.doi.org/10.1021/acsnano.6b02796.

[31] S.-W. Hsu, C. Ngo, A.R. Tao, Tunable and directional plasmonic coupling within semiconductor nanodisk assemblies, Nano Lett. 14 (5) (2014) 2372–2380, http://dx.doi.org/10.1021/nl404777h.

[32] B. Tandon, A. Agrawal, S. Heo, D.J. Milliron, Competition between depletion effects and coupling in the plasmon modulation of doped metal oxide nanocrystals, Nano Lett. 19 (3) (2019) 2012–2019, http://dx.doi.org/10.1021/acs.nanolett.9b00079.

[33] T.R. Gordon, T. Paik, D.R. Klein, G.V. Naik, H. Caglayan, A. Boltasseva, C.B. Murray, Shape-dependent plasmonic response and directed self-assembly in a new semiconductor building block, indium-doped cadmium oxide (ICO), Nano Lett. 13 (6) (2013) 2857–2863, http://dx.doi.org/10.1021/nl4012003.

[34] I. Kriegel, J. Rodríguez-Fernández, A. Wisnet, H. Zhang, C. Waurisch, A. Eychmüller, A. Dubavik, A.O. Govorov, J. Feldmann, Shedding light on vacancy-doped copper chalcogenides: Shape-controlled synthesis, optical properties, and modeling of copper telluride nanocrystals with near-infrared plasmon resonances, ACS Nano 7 (5) (2013) 4367–4377, http://dx.doi.org/10.1021/nn400894d.

[35] B. Tandon, S. Ghosh, D.J. Milliron, Dopant selection strategy for high-quality factor localized surface plasmon resonance from doped metal oxide nanocrystals, Chem. Mater. 31 (18) (2019) 7752–7760, http://dx.doi.org/10.1021/acs.chemmater.9b02917.

[36] B. Tandon, S.L. Gibbs, B.Z. Zydlewski, D.J. Milliron, Quantitative analysis of plasmonic metal oxide nanocrystal ensembles reveals the influence of dopant selection on intrinsic optoelectronic properties, Chem. Mater. 33 (17) (2021) 6955–6964, http://dx.doi.org/10.1021/acs.chemmater.1c01951.

[37] S.D. Lounis, E.L. Runnerstrom, A. Llordés, D.J. Milliron, Defect chemistry and plasmon physics of colloidal metal oxide nanocrystals, J. Phys. Chem. Lett. 5 (9) (2014) 1564–1574, http://dx.doi.org/10.1021/jz500440e.

[38] R. Borah, R. Ninakanti, S. Bals, S.W. Verbruggen, Plasmon resonance of gold and silver nanoparticle arrays in the Kretschmann (attenuated total reflectance) vs. direct incidence configuration, Sci. Rep. 12 (1) (2022) 15738, http://dx.doi.org/10.1038/s41598-022-20117-7.

[39] M.W. Berry, A.M. Green, B.J. Roman, T.M. Truskett, D.J. Milliron, Incorporating dopant effects in the plasmon ruler for metal-oxide nanocrystal superlattices, ACS Mater. Lett. 6 (5) (2024) 1929–1937, http://dx.doi.org/10.1021/acsmaterialslett.4c00220.

[40] C.-F. Chen, S.-D. Tzeng, H.-Y. Chen, K.-J. Lin, S. Gwo, Tunable plasmonic response from alkanethiolate-stabilized gold nanoparticle superlattices: Evidence of near-field coupling, J. Am. Chem. Soc. 130 (3) (2008) 824–826, http://dx.doi.org/10.1021/ja0773610.

[41] H. Matsui, T. Hasebe, N. Hasuike, H. Tabata, Plasmonic heat shielding in the infrared range using oxide semiconductor nanoparticles based on Sn-Doped In2O3: Effect of size and interparticle gap, ACS Appl. Nano Mater. 1 (4) (2018) http://dx.doi.org/10.1021/acsanm.8b00260.

[42] H. Matsui, S. Furuta, T. Hasebe, H. Tabata, Plasmonic-field interactions at nanoparticle interfaces for infrared thermal-shielding applications based on transparent oxide semiconductors, ACS Appl. Mater. Interfaces 8 (18) (2016) 11749–11757, http://dx.doi.org/10.1021/acsami.6b01202.

[43] L. Břínek, M. Kvapil, T. Šamořil, M. Hrtoň, R. Kalousek, V. Křápek, J. Spousta, P. Dub, P. Varga, T. Šikola, Plasmon resonances of mid-IR antennas on absorbing substrate: Optimization of localized plasmon-enhanced absorption upon strong coupling effect, ACS Photonics 5 (11) (2018) 4378–4385, http://dx.doi.org/10.1021/acsphotonics.8b00806.

[44] D. Ito, S. Yokoyama, T. Zaikova, K. Masuko, J.E. Hutchison, Synthesis of ligand-stabilized metal oxide nanocrystals and epitaxial core/shell nanocrystals via a lower-temperature esterification process, ACS Nano 8 (1) (2014) 64–75, http://dx.doi.org/10.1021/nn401888h.

[45] I. Hamberg, C.G. Granqvist, Evaporated Sn-doped In2O3 films: Basic optical properties and applications to energy-efficient windows, J. Appl. Phys. 60 (11) (1986) R123–R160, http://dx.doi.org/10.1063/1.337534.

[46] C.H.L. Weijtens, P.A.C. Van Loon, Influence of annealing on the optical properties of indium tin oxide, Thin Solid Films 196 (1) (1991) 1–10, http://dx.doi.org/10.1016/0040-6090(91)90169-X.

[47] T. Gerfin, M. Grätzel, Optical properties of tin-doped indium oxide determined by spectroscopic ellipsometry, J. Appl. Phys. 79 (3) (1996) 1722–1729, http://dx.doi.org/10.1063/1.360960.

[48] F. Kneizys, E. Shettle, L. Abreu, J. Chetwynd, G. Anderson, User guide to LOWTRAN 7, 1988, p. 146.

[49] M. Hirsch, LOWTRAN: Python module for atmospheric absorption modeling (v3.1), 2016, http://dx.doi.org/10.5281/zenodo.213475.

[50] J. Li, X. Ren, W. Yuan, Z. Li, G. Pei, Y. Su, C. Kutlu, J. Ji, S. Riffat, Experimental study on a novel photovoltaic thermal system using amorphous silicon cells deposited on stainless steel, Energy 159 (2018) 786–798, http://dx.doi.org/10.1016/j.energy.2018.06.127.

[51] E. Skoplaki, J.A. Palyvos, On the temperature dependence of photovoltaic module electrical performance: A review of efficiency/power correlations, Sol. Energy 83 (5) (2009) 614–624, http://dx.doi.org/10.1016/j.solener.2008.10.008.

[52] S. Dubey, J.N. Sarvaiya, B. Seshadri, Temperature dependent photovoltaic (PV) efficiency and its effect on PV production in the world – A review, Energy Procedia 33 (2013) 311–321, http://dx.doi.org/10.1016/j.egypro.2013.05.072.

[53] H. Matsui, M. Shoji, S. Higano, H. Yoda, Y. Ono, J. Yang, T. Misumi, A. Fujita, Infrared plasmonic metamaterials based on transparent nanoparticle films of In2O3:Sn for solar-thermal shielding applications, ACS Appl. Mater. Interfaces 14 (43) (2022) 49313–49325, http://dx.doi.org/10.1021/acsami.2c14257.

[54] W.J. Chang, B.J. Roman, A.M. Green, T.M. Truskett, D.J. Milliron, Surface-enhanced infrared absorption spectroscopy by resonant vibrational coupling with plasmonic metal oxide nanocrystals, ACS Nano (2024) http://dx.doi.org/10.1021/acsnano.4c06145.

[55] O. Zandi, A. Agrawal, A.B. Shearer, L.C. Reimnitz, C.J. Dahlman, C.M. Staller, D.J. Milliron, Impacts of surface depletion on the plasmonic properties of doped semiconductor nanocrystals, Nature Mater 17 (8) (2018) 710–717, http://dx.doi.org/10.1038/s41563-018-0130-5.

[56] A. Agrawal, I. Kriegel, D.J. Milliron, Shape-dependent field enhancement and plasmon resonance of oxide nanocrystals, J. Phys. Chem. C 119 (11) (2015) 6227–6238, http://dx.doi.org/10.1021/acs.jpcc.5b01648.

[57] A.M. Green, W.J. Chang, Z.M. Sherman, Z. Sakotic, K. Kim, D. Wasserman, D.J. Milliron, T.M. Truskett, Structural order and plasmonic response of nanoparticle monolayers, ACS Photonics 11 (3) (2024) 1280–1292, http://dx.doi.org/10.1021/acsphotonics.3c01813.

[58] K. Kim, J. Yu, J. Noh, L.C. Reimnitz, M. Chang, D.R. Gamelin, B.A. Korgel, G.S. Hwang, D.J. Milliron, Synthetic control of intrinsic defect formation in metal oxide nanocrystals using dissociated spectator metal salts, J. Am. Chem. Soc. 144 (50) (2022) 22941–22949, http://dx.doi.org/10.1021/jacs.2c08716.

[59] W.J. Chang, Z. Sakotic, A. Ware, A.M. Green, B.J. Roman, K. Kim, T.M. Truskett, D. Wasserman, D.J. Milliron, Wavelength tunable infrared perfect absorption in plasmonic nanocrystal monolayers, ACS Nano 18 (1) (2024) 972–982, http://dx.doi.org/10.1021/acsnano.3c09772.

[60] T.D. Dao, A.T. Doan, D.H. Ngo, K. Chen, S. Ishii, A. Tamanai, T. Nagao, Selective thermal emitters with infrared plasmonic indium tin oxide working in the atmosphere, Opt. Mater. Express, OME 9 (6) (2019) 2534–2544, http://dx.doi.org/10.1364/OME.9.002534.

[61] M. Pu, C. Hu, M. Wang, C. Huang, Z. Zhao, C. Wang, Q. Feng, X. Luo, Design principles for infrared wide-angle perfect absorber based on plasmonic structure, Opt. Express, OE 19 (18) (2011) 17413–17420, http://dx.doi.org/10.1364/OE.19.017413.

[62] K. Kim, Z.M. Sherman, A. Cleri, W.J. Chang, J.-P. Maria, T.M. Truskett, D.J. Milliron, Hierarchically doped plasmonic nanocrystal metamaterials, Nano Lett. 23 (16) (2023) 7633–7641, http://dx.doi.org/10.1021/acs.nanolett.3c02231.

[63] K. Dong, D. Tseng, J. Li, S. Warkander, J. Yao, J. Wu, Reducing temperature swing of space objects with temperature-adaptive solar or radiative coating, Cell Rep. Phys. Sci. 3 (10) (2022) 101066, http://dx.doi.org/10.1016/j.xcrp.2022.101066.

[64] T.S. Safi, J.N. Munday, Improving photovoltaic performance through radiative cooling in both terrestrial and extraterrestrial environments, Opt. Express, OE 23 (19) (2015) A1120–A1128, http://dx.doi.org/10.1364/OE.23.0A1120.

[65] G. Ulpiani, G. Ranzi, K.W. Shah, J. Feng, M. Santamouris, On the energy modulation of daytime radiative coolers: A review on infrared emissivity dynamic switch against overcooling, Sol. Energy 209 (2020) 278–301, http://dx.doi.org/10.1016/j.solener.2020.08.077.

[66] K. Ito, T. Watari, K. Nishikawa, H. Yoshimoto, H. Iizuka, Inverting the thermal radiative contrast of vanadium dioxide by metasurfaces based on localized gap-plasmons, APL Photonics 3 (8) (2018) 086101, http://dx.doi.org/10.1063/1.5025947.

[67] B. Tandon, S.L. Gibbs, C. Dean, D.J. Milliron, Highly responsive plasmon modulation in dopant-segregated nanocrystals, Nano Lett. 23 (3) (2023) 908–915, http://dx.doi.org/10.1021/acs.nanolett.2c04199.

[68] E. L. Runnerstrom, A. Llordés, S. D. Lounis, D. J. Milliron, Nanostructured electrochromic smart windows: traditional materials and NIR-selective plasmonic nanocrystals, Chem. Commun. 50 (73) (2014) 10555–10572, http://dx.doi.org/10.1039/C4CC03109A.

[69] G. Garcia, R. Buonsanti, E.L. Runnerstrom, R.J. Mendelsberg, A. Llordes, A. Anders, T.J. Richardson, D.J. Milliron, Dynamically modulating the surface plasmon resonance of doped semiconductor nanocrystals, Nano Lett. 11 (10) (2011) 4415–4420, http://dx.doi.org/10.1021/nl202597n.

[70] I. Kriegel, C. Jiang, J. Rodríguez-Fernández, R.D. Schaller, D.V. Talapin, E. da Como, J. Feldmann, Tuning the excitonic and plasmonic properties of copper chalcogenide nanocrystals, J. Am. Chem. Soc. 134 (3) (2012) 1583–1590, http://dx.doi.org/10.1021/ja207798q.

[71] A. Agrawal, I. Kriegel, E.L. Runnerstrom, F. Scotognella, A. Llordes, D.J. Milliron, Rationalizing the impact of surface depletion on electrochemical modulation of plasmon resonance absorption in metal oxide nanocrystals, ACS Photonics 5 (5) (2018) 2044–2050, http://dx.doi.org/10.1021/acsphotonics.7b01587.

[72] M. Ghini, N. Curreli, M.B. Lodi, N. Petrini, M. Wang, M. Prato, A. Fanti, L. Manna, I. Kriegel, Control of electronic band profiles through depletion layer engineering in core–shell nanocrystals, Nature Commun. 13 (1) (2022) 537, http://dx.doi.org/10.1038/s41467-022-28140-y.

[73] G.M. Paternò, C. Iseppon, A. D'Altri, C. Fasanotti, G. Merati, M. Randi, A. Desii, E.A.A. Pogna, D. Viola, G. Cerullo, F. Scotognella, I. Kriegel, Solution processable and optically switchable 1D photonic structures, Sci. Rep. 8 (1) (2018) 3517, http://dx.doi.org/10.1038/s41598-018-21824-w.

[74] Y. Jia, D. Liu, X. Wang, B. Cheng, H. Cheng, Dynamically modulating the mid-infrared localized surface plasmon resonance of Al-doped ZnO nanocrystals, Mater. Res. Express (2023) http://dx.doi.org/10.1088/2053-1591/acf43f.

[75] Y. Jia, D. Liu, D. Chen, Y. Jin, C. Chen, J. Tao, H. Cheng, S. Zhou, B. Cheng, X. Wang, Z. Meng, T. Liu, Transparent dynamic infrared emissivity regulators, Nature Commun. 14 (1) (2023) 5087, http://dx.doi.org/10.1038/s41467-023-40902-w.